

## 1. Properties of Energetic Ions and the Solar Atmosphere from Gamma-Ray Observations

Sum of contributions from R. Murphy, pieces from N. Vilmer, G. Hurford , G. Emslie so far

NOT TO BE DISTRIBUTED!!!

### 0.1. OVERVIEW OF GAMMA-RAY PHYSICS AND RELATIONSHIP TO SOLAR FLARE PHYSICS

Summary of theory and brief history of observations leading up to launch of RHESSI. The promise and impact of RHESSI on our understanding. (Nicole/Gerry/Ron) TO BE IMPLEMENTED Capabilities of RHESSI for improvement in understanding the ion component (David/Albert/Nicole). TO BE IMPLEMENTED Complementary neutron observations in space and on Earth TO BE IMPLEMENTED (Kyoko/Ron/Nicole).

### 0.2. CHARACTERISTICS OF FLARE LOOPS AND THEIR AFFECT ON GAMMA-RAY OBSERVATIONS

Most of the energetic particles that are accelerated in solar flares and interact with the solar atmosphere to produce observable emission are transported within magnetic loops. Evidence for this has come primarily from X-ray images of accelerated-electron bremsstrahlung which generally show emission from two sources. These source pairs have been interpreted as loop footpoints where the loop magnetic field penetrates the lower solar atmosphere and the ambient density is high enough for efficient production of radiation. There have been numerous examples of hard X-ray footpoint emission observed with several instruments such as SMM/HXIS, Hinotori, Yohkoh, and, most recently, RHESSI. Corresponding evidence for loop transport of accelerated ions has only come with the gamma-ray imaging possible with RHESSI. RHESSI observations of the 2003 October 28 flare clearly showed two sources of 2.223 MeV neutron-capture line emission. This line is produced by hydrogen capture of neutrons that result only from nuclear interactions of accelerated ions with the ambient solar atmosphere. The source pair is again interpreted as evidence for emission at the footpoints of a magnetic loop. Interestingly, the footpoints associated with the ion-produced emission were not coincident with the footpoints associated with the electron-produced bremsstrahlung emission, suggesting that ions and electrons were not accelerated and/or transported within the same loop.

Interactions of the accelerated ions produce excited and radioactive nuclei, neutrons and pi-mesons. All of these products subsequently produce observable gamma-ray emission via secondary processes and the neutrons that escape may be observed directly in space and on Earth and indirectly

via their decay protons. The measurable quantities associated with these emissions (e.g., gamma-ray line intensities, shapes, and time histories and escaping neutron spectra and time histories) convey information about the accelerated ions responsible for their production. This information is described by *acceleration parameters*, such as the number and spectral shape of the accelerated protons and  $\alpha$  particles (and thus their energy content) and the relative abundances of the accelerated ions, and can be obtained from measured deexcitation line intensities and ratios.

However, the measurable quantities can also depend strongly on the physical conditions of the magnetic flare loop in which the particles transport from the acceleration site to the interaction region. These physical conditions are described by *physical parameters*, such as loop length, the level of pitch-angle scattering (PAS) within the loop, the degree of convergence of the loop magnetic field at the footpoints, the location of the flare on the Sun, and the density and temperature height-profile and elemental composition of the flaring atmosphere. Analyses of high-energy solar-flare emissions therefore offer the potential to learn much more about the flare process than just particle acceleration, such as the structure and evolution of the flare environment.

But because each of the measurable quantities can depend on some or all of the same acceleration or physical parameters, deriving well-constrained values for those parameters is challenging. Analyses of flare gamma-ray data often have not taken these complicated inter-dependences into account in a systematic way, relying on *ad hoc* assumptions that resulted in unrealistically small uncertainties for their limited number of parameters. These inter-dependences were systematically addressed for the first time by Murphy et al. (2007) who identified all relevant parameters and showed how the various measurable quantities are affected by them.

In this section we discuss the physical parameters associated with ion transport in magnetic loops and how they affect the various measurable quantities.

#### 0.2.1. *Magnetic Loop Transport and Interaction Model*

A comprehensive understanding of the relationship between the physical conditions within the flare loop and the measurable quantities requires a model for ion acceleration, transport and interaction. Hua et al. (1989) developed a transport and interaction model that includes the most important aspects of loop transport. The model consists of a semicircular coronal portion of length  $L$  and two straight portions extending vertically from the transition region through the chromosphere into the photosphere. Below the transition region, the magnetic field strength is assumed proportional to a power  $\delta$  of the pressure (Zweibel et al. 1983). For coronal and photospheric pressures of 0.2 and  $10^5$  dyne  $\text{cm}^{-2}$  and relevant magnetic field strengths

of 100 and 1600 gauss, respectively,  $\delta \simeq 0.2$ . Such a converging magnetic field results in mirroring of accelerated particles. Pitch angle scattering is characterized by  $\Lambda$ , the mean free path required for an arbitrary initial angular distribution to relax to an isotropic distribution. The dependence of  $\Lambda$  on particle energy is expected to be weak (see discussion by Hua et al. 1989) and is assumed here to be independent. In the model, the level of PAS is characterized by  $\lambda$ , the ratio of  $\Lambda$  to the loop half-length  $L_c (= L/2)$ . Magnetic convergence and PAS directly affect the angular distribution of the accelerated particles when they interact with the ambient medium. This angular distribution will have a strong affect on the subsequent observable emissions. A specific height-density profiles ( $n(h)$ ) for the solar atmosphere is also assumed. Table 1 lists the acceleration and physical parameters of the loop transport and interaction model that affect the measurable quantities addressed by our calculations.

### 0.2.2. *Dependence of Nuclear Reactions on Loop Parameters*

Except for the neutrons that directly escape from the Sun, the immediate products of nuclear reactions (i.e., excited and radioactive nuclei, pions and the neutrons that remain at the Sun) are not directly observable but reveal themselves through secondary processes producing emissions that are observable (e.g., deexcitation gamma rays, annihilation gamma rays after positron emission, pion-decay radiation, and neutron-capture gamma rays). Before discussing how the loop parameters affect the measurable quantities, we must first understand how they affect the ions responsible for the nuclear interactions. The properties of an interacting accelerated ion that most significantly affect the measurable quantities associated with observable emission are (1) the time of the interaction after release from the acceleration region, (2) the ion direction of motion at interaction, (3) where in the loop the interaction occurs, and (4) the ion kinetic energy at interaction. The parameters listed in Table 1 combine to affect all of these properties to varying degree.

#### 0.2.2.1. *Time History*

The time history of the nuclear interaction rate is governed by both the time history of the ion acceleration release rate ( $a_{\text{ion}}(t)$ ) and transport in the loop. Here we will only consider the effects of transport, assuming instantaneous release of all particles at  $t = 0$ . In the absence of magnetic convergence ( $\delta = 0$ ), ions do not mirror and the nuclear interaction time history depends only on the energy loss rate in the lower chromosphere and upper photosphere where the density is greatest and most of the interactions occur. In the presence of magnetic convergence ( $\delta \neq 0$ ), ions with initial pitch angles lying close to the loop axis also do not mirror (they are within the “loss cone”) and behave similarly. Ions outside the loss cone mirror and lose energy much more slowly as they traverse the low-density corona. These

interactions thus occur on longer time scales, with the time scale increasing with increasing convergence. Pitch angle scattering causes the loss cone to be continuously repopulated. As a result, with increasing PAS (decreasing  $\lambda$ ) the nuclear interaction rate increases at early times and correspondingly decreases at later times. However, the time history is no longer affected by increasing PAS when the rate of loss-cone replenishment exceeds the rate of nuclear reactions in the loss cone. This saturation effect occurs for  $\lambda$  less than about 20. Increasing the loop length increases the time scale of the interaction rate since mirroring particles spend more time at lower coronal densities where nuclear reactions are less likely. The accelerated-ion spectral index has no significant affect on the interaction rate time history at times later than about 1 second after particle release. However, in harder spectra there is a larger fraction of ions with higher energies producing the reactions. Before about 1 second, this results in ions arriving earlier at the footpoints on their first transport down the loop leg. Similarly, the different energy dependences of the various interaction cross sections affect the time history only before about 1 second.

0.2.2.2. *Angular Distribution* In the absence of magnetic convergence ( $\delta = 0$ ), there is no mirroring and the angular distribution of the interacting ions (in the loop model, initially assumed isotropic when released at the top of the loop) will be downward isotropic regardless of level of PAS or loop size. In the presence of magnetic convergence ( $\delta \neq 0$ ) but no PAS, ions with pitch angles too small to mirror enter the “loss cone” and either undergo a nuclear reaction as they are moving downward or are thermalized. But most ions have larger initial pitch angles which results in mirroring and the interactions occur mostly at the ion mirror points where the density is greatest. Thus, most ions are moving parallel to the solar surface when they interact (i.e., a “fan beam” angular distribution; see, e.g., Hua et al. 1987b) with a relatively small contribution from downward-moving ions. The downward contribution becomes even less important as  $\delta$  increases. PAS repopulates the loss cone so that as PAS is increased ( $\lambda$  decreased), more ions interact in the loss cone and the distribution becomes more downward-directed until saturation is reached ( $\lambda \simeq 20$ ). The angular distribution of the accelerated ions when they interact is not significantly affected by the spectral index or the energy dependence of the interaction cross section.

0.2.2.3. *Depth Distribution* In the absence of magnetic convergence ( $\delta = 0$ ), there is no mirroring and the depth distribution directly reflects the grammage required for the accelerated ions to interact as they move downward through the solar atmosphere. In the presence of magnetic convergence ( $\delta \neq 0$ ), mirroring results in interactions occurring at higher elevations (and therefore lower densities) as more and more particles are prevented from

penetrating the lower atmosphere. Even with minimal convergence, the lack of PAS results in a significant fraction of the interactions occurring at low densities (almost 20% of the interactions occur at densities less than  $10^{10}$  H  $\text{cm}^{-3}$ ). As PAS is increased ( $\lambda$  decreased), the bulk of the interactions move deeper to higher densities as more interactions occur within the loss cone. Because higher-energy ions tend to interact farther along their paths, harder particle spectra result in interactions occurring at higher densities since more higher-energy ions are producing the interactions. Similarly, interactions whose cross sections have high threshold energies tend to interact at higher densities. This dependence of the depth distribution on the interaction cross section also explains why the depth distribution is affected by the accelerated  $\alpha$ /proton ratio. Alpha-particle interactions generally have lower threshold energies and, as just discussed, such interactions occur at lower densities. When the  $\alpha$ /proton ratio is high, a larger fraction of the line yield is due to such reactions and the depth distribution shifts to lower densities.

*0.2.2.4. Effective Energies of the Accelerated Ions Producing Gamma Rays and Neutrons* In later sections we will explore the dependences of various measurable quantities of flare emissions on the acceleration and physical parameters. When deriving these parameters from the measurements, it is important to be aware that each observable is sensitive only to a unique range of accelerated-ion energies. The main factor determining the effective energy range for a nuclear reaction is the cross section, but the shape of the accelerated-ion spectrum can be important. Steep spectra shift the emphasis to lower energies and vice versa. For thin target interactions, only ions with energies where the cross section is significant contribute. For thick target interactions, however, even ions with high energies where cross sections are often small also contribute, since they can lose energy and then interact at energies where the cross section is significant.

The differential energetic-ion kinetic energy spectrum gives the number of ions accelerated per unit energy at each energy. To determine the effective ion energies for a particular ion spectrum, we weight yields from monoenergetic ions with the spectrum. As an example, we show in Figure 1 the differential yield of the 1.634 MeV  $^{20}\text{Ne}$  line as a function of accelerated ion energy for power law spectra with indexes of 3 and 5 and accelerated  $\alpha$ /proton = 0.5. (We emphasize that these energies are those of the ions leaving the acceleration region.) We show the separate contributions to the line from accelerated protons (dashed curves) and alpha particles (dotted curves). We see that for soft spectra, the  $\alpha$ -particle contributions dominate due their lower threshold energies, and the most effective ion energies are around a few MeV nucleon $^{-1}$ . For hard spectra, the proton interactions become important due to their higher threshold energies and the effective energies are higher. For intermediate spectral indexes, both accelerated par-

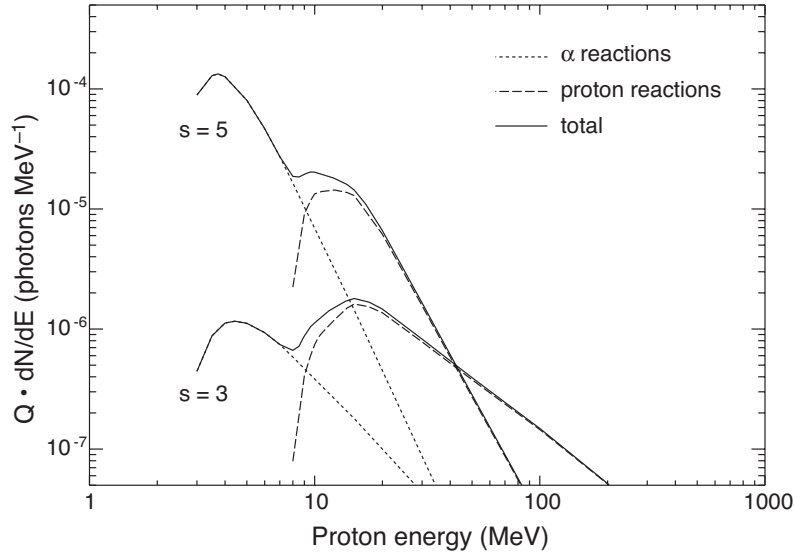


Figure 1. Yield of the 6.129 MeV  $^{16}\text{O}$  line weighted by accelerated ion power law spectra with indexes  $s = 3$  and 5. The contribution to the line from accelerated protons and  $\alpha$  particles are separately shown.

ticles can be important and the effective ion energy range can be very broad. To quantify the effective ion energy range for producing the line, we use the following definition: we identify the ion energy where the yield is maximum, and then define the effective range to be that within which the yield has fallen to 50% on each side of the maximum. We note that if the effective energy distribution is very broad, the arbitrary value of 50% could be misleading.

The fluence ratio of the 6.129 MeV  $^{16}\text{O}$  and 1.634 MeV  $^{20}\text{Ne}$  lines has been frequently used as a measure of the accelerated-ion spectral index. Using the 50% definition for the effective accelerated-ion energy range as given above, we can now see what ion energies are most relevant to this ratio. We show in Figure 2 the effective accelerated-ion energy ranges for producing the 1.634 MeV  $^{20}\text{Ne}$  line (white boxes) and the 6.129 MeV  $^{16}\text{O}$  line (grey boxes) for several power law spectral indexes and for accelerated  $\alpha$ /proton = 0.1 (panel a) and 0.5 (panel b). The horizontal line within each box corresponds to the peak of the distribution. The Figure shows that the effective energy range for producing the  $^{16}\text{O}$  line is always shifted to energies higher than for the  $^{20}\text{Ne}$  line. The extent of the separation of the effective energy ranges for the two lines determines the sensitivity of the ratio to the spectral index. Because the separation for these two lines is not large, the ratio is not very sensitive. For very hard spectra, the upper range of the effective ion energies can be  $\sim 100$  MeV nucleon $^{-1}$ . But for most (softer)

spectra it is less than  $10 \text{ MeV nucleon}^{-1}$ . The lower range is typically a few  $\text{MeV nucleon}^{-1}$  but for very soft spectra (particularly when  $\alpha/\text{proton} = 0.5$ ) it can be less than  $2 \text{ MeV nucleon}^{-1}$  when the line production is dominated by the lower-energy reactions of accelerated  $\alpha$  particles. As the spectrum hardens, the higher-energy proton reactions begin to contribute and the effective ion energy range shifts to higher energies and becomes broader as interactions of both  $\alpha$  particles and protons contribute.

The fluence ratio of the  $4.438 \text{ MeV } ^{12}\text{C}$  deexcitation line and the  $2.223 \text{ MeV}$  neutron-capture line has also been used as a measure of the accelerated-ion spectral index. We show in Figure 3 the effective accelerated ion energy ranges for the  $4.44 \text{ MeV}$  line (white boxes) and the  $2.223 \text{ MeV}$  line (grey boxes) for several power law spectral indexes and for accelerated  $\alpha/\text{proton} = 0.1$  (panel a) and  $0.5$  (panel b). The ranges of effective ion energy ranges for the  $4.44 \text{ MeV}$  line are similar to those for the  $6.129 \text{ MeV } ^{16}\text{O}$  line shown in Figure xx since the production cross sections for the two lines are similar. For hard spectra ( $s < 4$ ), the effective ion energies for the neutron capture line extend to very high energies, up to  $100 \text{ MeV nucleon}^{-1}$ , and are generally much higher than those producing the  $^{12}\text{C}$  line. However, for soft spectra ( $s > 4$ ), the effective ion energies for the neutron capture line can be very low ( $< 7 \text{ MeV nucleon}^{-1}$ ) due to neutron production by the exothermic ( $\alpha, n$ ) reactions on heavy elements. For such soft spectra the effective ion energies for the neutron capture line are even less than those for the  $^{12}\text{C}$  line. We find that there is essentially no dependence of the neutron capture line effective ion energy ranges on  $\lambda$  and  $\delta$ . As the flare location moves from disk center to limb, the effective energies shift to slightly lower energies since the neutrons from higher energy reactions are generally produced deeper and are subsequently more attenuated by Compton scattering. When a spectral index is derived using the ratio of these two lines, the relevant ion energies cover a broad range of energies. For hard spectra, the relevant ion energy range extends from a few  $\text{MeV nucleon}^{-1}$  up to and greater than  $100 \text{ MeV nucleon}^{-1}$ . For soft spectra ( $s > 4$ ), the relevant ion energy range is much narrower, from less than 1 to a few  $\text{MeV nucleon}^{-1}$ . For very soft spectra, the lack of separation of the effective ion energies producing the two lines reduces the sensitivity of the ratio to the spectral index.

Determining the effective accelerated ion energies for production of the neutrons escaping from the Sun...

In Figure 4 we show the effective accelerated ion energies for the production of positrons for accelerated  $^3\text{He}/^4\text{He} = 0$  (white boxes) and 1 (grey boxes) and for accelerated  $\alpha/\text{proton} = 0.1$  (panel a) and  $0.5$  (panel b). The figure shows that for very hard spectra, the effective ion energies can be extend to more than a  $\text{GeV nucleon}^{-1}$  because the positrons result mainly from very high-energy reactions producing charged pions. With  $\alpha/\text{proton} = 0.1$ , the production is primarily from accelerated proton reactions and the lower

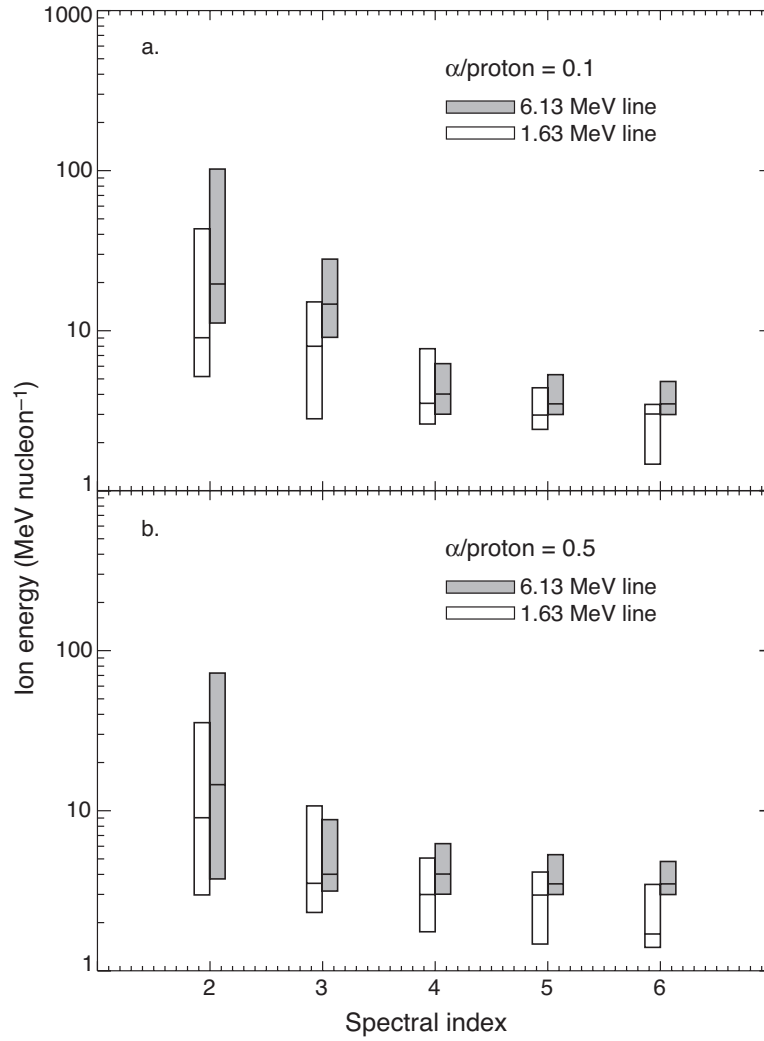


Figure 2. Effective accelerated ion energies for production of the 1.634 MeV  $^{20}\text{Ne}$  line (white boxes) and 6.129 MeV  $^{16}\text{O}$  line (grey boxes) as a function of spectral index. The effective energy ranges are the 50% yield range as defined in the text. Panel a is for accelerated  $\alpha/\text{proton} = 0.1$  and panel b is for 0.5.

energy of the effective energy range is several hundred MeV nucleon<sup>-1</sup>. When  $\alpha/\text{proton}$  is 0.5, lower energy accelerated  $\alpha$  particle interactions producing radioactive nuclei also contribute, extending the effective energy range to lower energies. The very low energy reactions of accelerated  $^3\text{He}$  do not contribute significantly for hard spectra. For softer spectra, the contribution from  $^3\text{He}$  reactions can lower the lower range of the effective energies to less

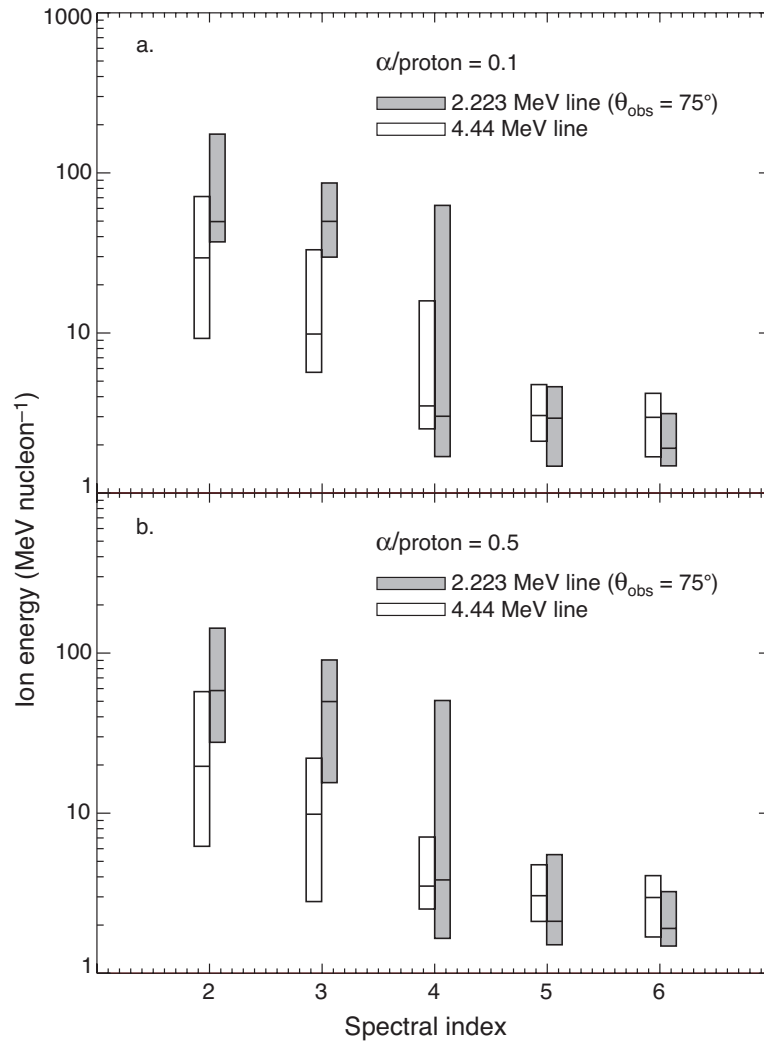


Figure 3. Effective accelerated ion energies for production of the 4.438 MeV  $^{12}\text{C}$  line (white boxes) and 2.223 MeV neutron capture line (grey boxes) as a function of spectral index. The effective energy ranges are the 50% yield range as defined in the text. Panel a is for accelerated  $\alpha/\text{proton} = 0.1$  and panel b is for 0.5. For the neutron capture line,  $\lambda = 300$ ,  $\delta = 0.2$ ,  $L = 11,500$  km, and  $\theta_{\text{obs}} = 75^\circ$ .

than 1 MeV nucleon<sup>-1</sup>, the lowest ion energies for any of the observables considered here. The upper range is from a few MeV nucleon<sup>-1</sup> to  $\sim 15$  MeV nucleon<sup>-1</sup> depending on the  $^3\text{He}$  abundance. We also show in Figure xx the effective accelerated ion energy ranges for the 4.44 MeV line from Figure xx. We see that when spectral indexes are determined from this ratio, the effective ion energies are from less than an MeV nucleon<sup>-1</sup> to a few MeV

nucleon<sup>-1</sup> for very soft spectra and from many MeV nucleon<sup>-1</sup> to over a GeV nucleon<sup>-1</sup> for very hard spectra. We again caution, however, that the effective energies shown in this figure are for the production of *positrons*. The escaping 0.511 MeV annihilation photons can be significantly attenuated if the positrons are produced deep in the solar atmosphere. Pion production can be very deep since the high energy ions responsible have very long ranges. As a result, even for very hard spectra, the annihilation photons that escape can be mainly from decay of radioactive nuclei rather than pions. Such nuclei are produced by ions with energies that are much lower than those indicated in the figure. High-energy (>10 MeV) continuum emission from neutral and charged pion decay is only produced by accelerated ions (protons and  $\alpha$  particles) with energies greater than  $\sim 200$  MeV nucleon<sup>-1</sup>.

### 0.2.3. *Effect of the Loop Parameters on the Observable Quantities*

#### 0.2.4. *Peak time delays and Loop Parameters*

Peak time delays have been reported in a few flares between hard X-rays and gamma-ray line emissions (e.g. Hulot et al., 1989 others?). Zweibel and Haber (1983) computed gamma-ray emissions from flares, taking into account the propagation of energetic ions in magnetic loops. They showed that the mirror force traps a large fraction of the accelerated particles in the corona. The removal time of the protons from the loops is then quite long and leads to extended time profiles of the gamma-ray production inconsistent with the very impulsive commonly observed time profiles. Zweibel and Haber pointed out however that if in addition to magnetic mirroring, pitch-angle scattering resulting from MHD turbulence is taken into account, then the decay time of the gamma-ray emission from trapped plus precipitated protons is consistent with the observed ones. Following this approach, Hua et al. (1989) computed the time dependence of the nuclear line production from ions in a magnetic loop taking into account energy losses due to Coulomb collisions, removal by nuclear reactions, magnetic mirroring and MHD pitch-angle scattering. (RON'S Part ....)

The relative timing of prompt gamma-ray line emissions and of hard X-rays was studied by Hulot and collaborators (1989) and discussed in the context of trap plus precipitation models. These models were used to interpret the delays of the hard X-ray and gamma-ray line emissions observed for two flares by ISEE-3 and SMM/GRS (Hulot et al., 1992) and also applied to one of the gamma-ray line flare observed with RHESSI.

The basic characteristics of the hard X-ray and gamma-ray trap plus precipitation models are presented in Vilmer et al. (1982) and Hulot et al., (1989). The principle of the model is the following: electrons and ions are supposed to be continuously injected over a finite injection time in a coronal loop of mean density  $n_0$  in which they are partially trapped. The magnetic field in the loop is supposed to be constant. A strong increase of the magnetic

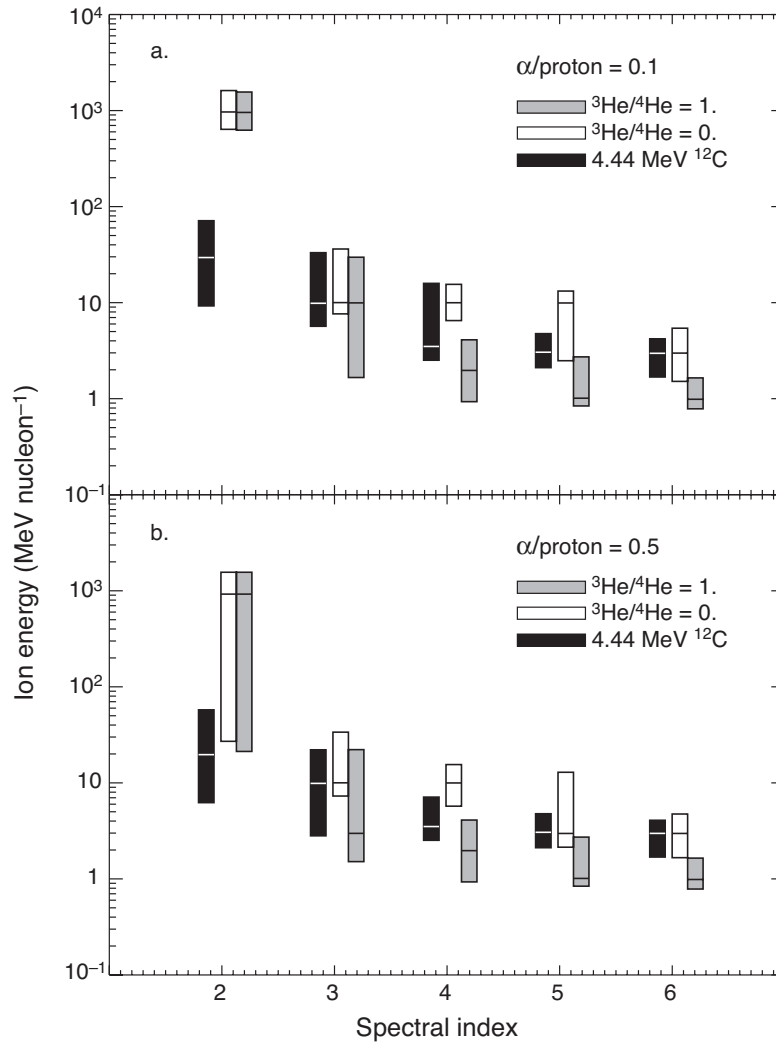


Figure 4. Effective accelerated ion energies for production of positrons as a function of spectral index for accelerated  ${}^3\text{He}/{}^4\text{He} = 0$  (white boxes) and 1 (grey boxes). The effective energy ranges are the 50% yield range as defined in the text. Panel a is for accelerated  $\alpha/\text{proton} = 0.1$  and panel b is for 0.5. Also shown are the effective energies for the 4.438 MeV  ${}^{16}\text{O}$  line (black boxes) from Figure 3.

field and of the density at the bottom of the loop leads to partial particle trapping and to the formation of a loss cone ( $\alpha_0$ ). Particle energy losses in the corona are assumed to be due only to Coulomb collisions. While particles trapped in the loops produce X-ray and gamma-ray thin target emissions, electrons and protons escaping from the trap propagate downwards to the

denser chromospheric layers where they produce hard X-ray and gamma-ray line emissions in a thick target approximation. In these works, the precipitation rate is supposed to be in the 'strong diffusion limit' defined by e.g. Kennel and Petschek (1966) (the precipitation mechanism saturates, due to strong scattering by turbulence in the corona, the distribution in the loop is mostly isotropic and the loss cone is continuously replenished). In these conditions, the precipitation rate is simply related to the convergence of the magnetic field from the corona to the chromosphere and thus to the geometric size of the loss cone.

TO BE FINISHED BY NICOLE AND REORGANIZED WITH RONS  
TEXT

### 0.3. IMAGING SOLAR GAMMA-RAYS

(Gordon Hurford-DRAFT )

INCOMPLETE DRAFT FROM G. HURFORD NOT FOR DISTRIBUTION

#### 0.3.1. *Introduction*

The spatial distribution of gamma-ray emission provides a channel of information on the acceleration and transport of energetic ions that is independent of spectroscopic analyses. As with electron-bremsstrahlung, nuclear gamma-rays disclose not where the particle acceleration occurs, but rather where accelerated particle interacts with the ambient atmosphere. Nevertheless it provides the only available method that can place accelerated ions in a solar magnetic context.

Prior to the launch of RHESSI, the only information on the spatial distribution of solar flare gamma-ray emission was a report by Vestrand and Forrest (19xx) of neutron-capture line emission from a flare that was believed to be behind the limb. Such an observation would imply that the gamma-rays emanated from a source, perhaps diffuse, that was far from the flare itself. \*\*\*\*\*IS THERE A PUBLISHED FOLLOWUP ON THAT PAPER?\*\*\*\*\*

RHESSI gamma-ray imaging to date is based mainly on the narrow neutron-capture line at 2.223 MeV. This line generated when fast neutrons, created by the interaction of accelerated protons and ions with the ambient atmosphere, are thermalized and subsequently captured by protons, producing deuterium and a narrow gamma-ray line at 2.223 MeV. Narrow because of the absence of Doppler broadening, the line is the optimal choice for imaging for four reasons: it is relatively intense; there is no locally-generated background line emission (since locally-generated fast neutrons cannot thermalize in the limited mass of the spacecraft.); the line is narrow so that the continuum background is minimized; the narrowness of the line

also limits the contribution of the solar electron-bremsstrahlung continuum to the resulting images. The multiple elastic collisions required for neutron thermalization typically take 100 seconds (reference needed), which results in a characteristic time delay in this line compared to the prompt lines. Modeling also indicates that the average distance traveled by the neutron during this process is 500 km (reference). As a result, despite its two-step formation mechanism, a neutron-capture line image faithfully indicates of the site of the original nuclear interaction to within an arcsecond.

RHESSI imaging of nuclear gamma-ray emission is based on data from the thick rear-segments of RMCs 6 and 9 (35 and 183 arcsec resolution respectively), the only RMCs for which the grids are sufficiently thick to modulate the high energy flux. The rear segments of the detectors are shielded from the intense flux of low energy x-rays, and so potential concerns about instrumental live time or pulse pileup effects (Smith et al 2002) are not a significant factor. On the other hand, since only two of the nine RMCs are relevant to imaging, the gamma-ray throughput for such imaging is only about 15

??????DO WE NEED THIS HERE OR ELSEWHERE?????? RHESSI data is in the form of time- and energy-tagged counts, imaging is based on selecting events which satisfy user-selected time and energy criteria. Combined with accurate aspect information, the selected events are then used to reconstruct the image of the source using algorithms such as back-projection (Hurford et al 2002). Although limited in its ability to reproduce complex source morphologies, such imaging is well-suited to quantitative characterization of simple sources.

### 0.3.2. *Neutron-capture Line Imaging*

The complete set images obtained to date is shown in Figure 1 with quantitative details summarized in Table 1 (Hurford et al. 2003, 2006, 2007). Rather than deal with each flare in turn, we summarize these observations from three perspectives: the number of distinct components; their size; and their location.

Considering first the number of distinct components, four of the five events presented a single, unresolved source whereas the fifth event, 28 October 2003, showed a double source that straddled an arcade of loops. This pattern does not necessarily imply that double footpoint sources are an atypical feature of gamma-ray emission. Two conditions must be met to image a double footpoint source: the separation of the footpoints must be sufficiently large that they can be resolved with the available resolution; and there must be sufficient signal-to-noise that sources two (rather than one) can be confidently detected. Referring to Table 1 and using the separation of the electron-bremsstrahlung components as a guide, the October 28 event was the only one of the five that satisfied both criteria and that event did

display a double source. Had gamma-ray emission from the other events also been in the form of double sources, it could not have been observed. Thus there is no evidence from the number of components to suggest that the true neutron-capture line sources are predominantly single sources, in contrast to typical hard x-ray double sources.

A second perspective is provided by the estimates of the size of the unresolved components. Such estimates can be obtained from comparisons of the total observed line flux to that imaged in the unresolved source. The ratio of imaged to total flux, called the relative visibility, can be used to put useful limits on the size of an unresolved source. Ignoring the modulation, the total number of observed counts in the line provides a direct indication of the spatially integrated flux in the narrow energy range associated with the line. Such counts are due to a combination of real solar neutron-capture line events, solar and continuum background. Since the number of such counts that are due to solar or background continuum can be reliably estimated from energy ranges just above 2.223 MeV, an accurate determination of the spatially integrated solar neutron-capture line flux can be made, independent of background models. The imaged flux does not contain any unmodulated background, but could include a contribution from the solar continuum. Although this contribution could be estimated by imaging in a narrow energy range above 2.223 MeV, it is easily demonstrated that, thanks to the narrow energy range required for imaging the neutron-capture line (10-14 keV, Table 1), its contribution is negligible. Note that since the relative visibilities are estimated by comparing the imaged to total counts observed with a given detector, the result is independent of any errors in estimating the detector efficiency.

The observed relative visibilities (Table 1), show that in all cases the flux in the unresolved neutron-capture line source(s) is consistent with the spatially-integrated flux. This implies that there is no evidence for a large-scale diffuse component. Alternatively, by assuming a Gaussian source model, upper limits to the FWHM source diameters are obtained that correspond to a few 10s of arcseconds.

A third perspective on the neutron-capture line sources is provided by their location. An unanticipated result in this case was that in some, if not all, cases, the neutron-capture line sources were not co-spatial with the corresponding electron-bremsstrahlung sources. Since the character and statistical significance of the displacements differed from event-to-event, we first consider them individually. For the 28 October 2003 event, the double footpoint sources straddled the same loop arcade as the electron sources but were displaced along the loop arcade by 14-15+-xxx arcseconds (Figure 1). For the other events, the location of the single unresolved sources are expressed as a centroid location with appropriate statistical errors. For the July 2003 event each of neutron-capture line source was displaced by 25+-

5 arcseconds from the corresponding electron source. Although it was not located near any obvious EUV or H-alpha line emission, its location was consistent with the footpoint of a post-flare loop. For 20 January 2005 the neutron source was clearly associated with one of the two electron-bremsstrahlung footpoints. For 2 November 2003 the location also appeared to be preferentially associated with one of the two electron-bremsstrahlung footpoints, although in this case, the displacement of the 2.2 MeV emission compared to the centroid of the electron-bremsstrahlung source was significant only at the 2-sigma level. For the 5th event, the measured separation of the corresponding centroids was  $\pm$ xxx arcseconds, so a separation, if any, could not be established. In summary, statistically significant displacements were observed in three of the five events, marginally in a fourth but not seen in the fifth and statistically least significant event.

### 0.3.3. *Other Gamma-ray Imaging*

In addition to the neutron-capture line, imaging of the gamma-ray continuum has also been reported (Hurford et al 2005, 2007). At the higher energies, where broad nuclear emission is more important, only RMC 9 (183 arcseconds) was effective with the events studied. The preliminary explanation for this is that photons passing through front grid slits into rear grid slats could scatter into the detector and be counted as part of the modulated flux. Such events, however, are 180 degrees out of phase with the true (front slit-to-rear slit) events and so tend to reduce the effective modulation efficiency. This issue is only a factor for grid 6 whose grids are not thick enough to suppress the scattered photons. It is not relevant for neutron-capture line imaging since the energy of the scattered photons is reduced.

Nevertheless the centroid locations obtained for the 20 January 2005 event gamma-ray continuum were of interest. In particular, the centroid locations were energy dependent (Figure 2), Matching the centroid of the electron-bremsstrahlung source at lower energies, but trending toward the neutron-capture line centroid at higher energies where the nuclear contribution became more important. Such a trend provides independent confirmation of the displacement between the sites of electron-bremsstrahlung collisions and nuclear interactions.

Preliminary results of imaging in a narrow energy range surrounding the 511 keV line also became available for the 20 January 2005 event. Images obtained independently from the front and rear segments of RMC9 were self consistent in terms of strength and intensity. However, modeling suggests that although a narrow xxx-yyy keV range was used, the band was dominated by the electron-bremsstrahlung continuum, at least for this event.

\*\*\*\*\*DISCUSSION OF INTENSITIES?\*\*\*\*\*

#### 0.3.4. *Discussion*

One well-established result of the neutron-capture line imaging was that the neutron-capture line flux for all five events, was consistent with coming from compact source component(s) in the flaring active region. This would tend to suggest that the flare-associated gamma-ray emission was associated flare-accelerated ions, as opposed to ions that were shock-accelerated at high altitudes, which might be expected to interact with ambient material in a more diffuse pattern, diffuse perhaps some distance from the flare.

Given the resolution and sensitivity of the imaging and the limited sample of events, there is no evidence yet that the morphology of nuclear gamma ray sources (e.g. double vs single footpoints) differs systematically from that of hard x-ray sources.

The most striking result is of course, the differences in the locations of the electron-bremsstrahlung and neutron-capture line sources. Hypotheses that attempt to account for such results generally fall into three categories: i: that the displacement is an instrumental artifact; ii: that the displacement has a solar, but relatively mundane origin; or iii: that the displacement reflects a difference in acceleration and/or transport processes for flare-accelerated ions and electrons.

Since spatial displacements between the electron-bremsstrahlung and neutron capture line sources were an unanticipated feature, we first consider the possibility that the displacements are an artifact of the mapping process. There are three independent arguments that suggest this is highly unlikely. First, in comparing the locations of the sources at two different energy regimes, the comparisons were based on analyses that differed only in the energy of the counts upon which the imaging is based. The same time interval, RMCs, aspect solution and imaging algorithm and parameters were used so that the potential for systematic co-location errors could be discounted. Second, if the relative displacements were of systematic instrumental origin they would likely be with respect to the only axis of symmetry associated with the mapping process, namely the line joining the direction of the rotation axis to that of the flare. However, the displacements were neither systematically radial nor azimuthally displaced relative to this direction. Third, in all but the 23 July 2002 event, the direction of the displacement, if any, was in a solar-magnetically significant as opposed to randomly-chosen direction. As result of these three considerations, it is considered highly likely that the displacements have a solar origin.

A second class of potential explanations for the displacements is that they have a solar, but relatively mundane explanation. One such explanation might be the displacement between the locations of the original nuclear interaction and that of the neutron-capture process. However, as mentioned, modeling indicates that such a displacement is less than 1 arcsecond. Another possibility is that the displacement is related to the time-delay asso-

ciated with thermalization. This scenario is notes that the neutron-capture line image reflects the location of nuclear interactions that occurred 100 seconds earlier. To test this hypothesis, for each event, the neutron-capture line images were compared to both cotemporaneous electron-bremsstrahlung images both with the same and with a 100 second earlier integration times. No significant difference was observed.

Turning to more solar-based explanations, a hypothesis that

Conclusions

Displacement issue unresolved ???Propagation modeling??? Need more events to establish systematics Statistical and angular resolution limitations Inspirational call for more data

### 0.3.5. *Interpretation*

In the stochastic acceleration model of Miller and Roberts (1995) and Miller, LaRosa, & Moore (1996), particles are accelerated through *second-order resonant Fermi acceleration*. Magnetic compressions associated with fast-mode MHD waves propagating at an angle to the magnetic field constitute the scattering centers. Therefore, in order to act as an efficient particle accelerator, the test particle must have an initial speed that is greater than the speed of the magnetic compression, i.e., of order the Alfvén speed. For the pre-flare solar corona, *electrons* have speeds comparable to, or greater than, the Alfvén speed, and so are efficiently accelerated immediately. On the other hand, in a low- $\beta$  plasma the protons necessarily have an initial speed that is less than the Alfvén speed and so are not efficiently accelerated: the scattering centers converge before the test particle has suffered a sufficient number of energy-enhancing collisions. Efficient acceleration of ions therefore requires pre-acceleration to Alfvén speeds.

In the model of Miller and Roberts (1995), this pre-acceleration is accomplished through (parallel-propagating) Alfvén waves, and it is essential to realize that *this process takes some time to accomplish*. During this pre-acceleration period  $\tau_{\text{pre-acceleration}}$ , most of the energy is deposited in accelerated electrons; only after the protons are pre-accelerated to the Alfvén speed are they effectively accelerated – they then gain the bulk of the released energy by virtue of their greater mass (Miller and Roberts 1995).

It therefore follows that if the timescale  $\tau_{\text{escape}}$  for protons to escape the acceleration region satisfies  $\tau_{\text{escape}} \ll \tau_{\text{pre-acceleration}}$ , then no effective proton acceleration occurs. (Conversely, if  $\tau_{\text{escape}} \gg \tau_{\text{pre-acceleration}}$ , then efficient ion acceleration occurs.) Emslie, Miller, & Brown (2004; equation [7]) have shown that the above inequality may be written as

$$\frac{B_2^2}{L_9 Q_2^{2/3} n_{10}^{1/2}} 15, \quad (1)$$

where  $B_2$  and  $n_{10}$  are the ambient magnetic field ( $10^2$  G) and density ( $10^{10}$  cm $^{-3}$ ),  $L_9$  is the acceleration region length ( $10^9$  cm), and  $Q_2$  is the volumetric rate of energy input ( $10^2$  ergs cm $^{-3}$  s $^{-1}$ ). Thus a suitable combination of (1) large loop length  $L$ , (2) low ambient magnetic field  $B$ , high density  $n$  and high rate of energy deposition  $Q$  will lead to a preference for ion acceleration and so gamma-ray emission.

Observations of the 2002 July 23 flare (Hurford et al. 2003) have suggested that the ions are accelerated on longer field lines, consistent with the above explanation. The interpretation of time delays between gamma-ray lines and hard X-rays by trap plus precipitation models for the same flare (Dauphin and Vilmer, 2007) confirm the fact that ions are injected in longer loops than electrons.

In other events (e.g. 2005 January 20), such a differentiation of loop lengths is not as apparent, and so one must resort to different values of  $B$ ,  $n$ , or  $Q$  on different field lines to account for the observed separation of gamma-ray- and hard X-ray-emitting regions.

#### 0.4. FLARE-ACCELERATED ION COMPOSITION, SPECTRA, AND TRANSPORT

##### 0.4.1. *History of the early observations and theoretical developments leading up to the launch of RHESSI: Composition of the Heavy Accelerated Ions*

The relative abundances of accelerated ions heavier than He can be determined from the relative fluences of the broad deexcitation lines. These lines are produced when such heavy energetic ions interact with ambient H and He. Because the heavy ions lose little of their kinetic energy in the reactions, the excited nucleus produced has a large velocity and the deexcitation gamma ray can be strongly Doppler broadened by up to  $\sim 20\%$  full width at half maximum (FWHM). Because the lines are so broad, many of them overlap, making the heavy-ion abundance determination much more difficult than the corresponding determination of ambient abundances using the narrow deexcitation lines. In addition, such broad lines are difficult to distinguish from the underlying continua from electron bremsstrahlung and the nuclear continuum. The nuclear continuum is composed of hundreds of relatively-weak, close-spaced deexcitation lines that also result from the nuclear interactions along with the strong lines clearly visible in flare spectra. These lines are so numerous and closely spaced that they merge and appear as a continuum to gamma-ray detectors. This continuum, however, does have structure, on the order of several hundred MeV, and knowledge of this structure is critical to reliably separate it from the broad lines. The early attempts to derive heavy-ion abundances from flare gamma-ray data that we discuss here used relatively crude modeling of this nuclear continuum.

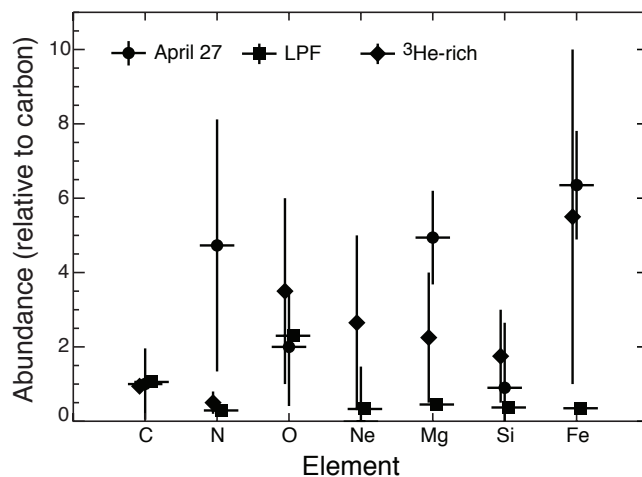


Figure 5. Derived accelerated-ion abundances relative accelerated C (circles). Also shown are large proton flare (LPF, squares) and impulsive <sup>3</sup>He-rich event (diamonds) abundances

On-going analyses using improved nuclear-continuum modeling recently obtained from modern nuclear reaction codes will improve the reliability of such determinations.

Murphy et al. (1991) used the gamma-ray deexcitation line code (Ramaty et al. 1979; Kozlovsky et al. 2002) to calculate both narrow and broad line spectra for the most abundant elements in the solar atmosphere and the accelerated ions. The abundances were varied to obtain the best fit to the *SMM* data for the 27 April 1981 flare. The resulting accelerated-ion abundances relative to accelerated C are shown in Figure 5. Also shown for comparison are similar element abundances measured in space from large proton flares (LPF) and impulsive, <sup>3</sup>He-rich events. The uncertainties for most of the elements are quite large, but Mg and Fe are seen to be significantly ( $>3\text{--}4\sigma$ ) enhanced relative to C and O, similar to the enhancements seen in the impulsive <sup>3</sup>He-rich events. Neither

TO ADD SOME OBSERVATIONS FROM GRANAT (Nicole)

#### 0.4.2. *History of the early observations and theoretical developments : High Energy Emissions in Solar Flares*

Observations of energetic neutrons and of pion decay radiation from solar flares combined with observations of de-excitation gamma-ray lines give a complete picture of the accelerated ion distribution above a few MeV/nucleon up to several GeV/nucleon (e.g. Chupp 1984, Chupp, 1996, Ramaty, 1996, Vilmer and MacKinnon, 2003 for reviews). Studies of high energy emissions from the flare site started with *SMM* (Murphy et al., 1987), continued with events observed with *GAMMA1* (Akimov et al., 1992), *CGRO* (e.g.

Mandzhavidze and Ramaty 1992; Kanbach et al., 1993; Dunphy et al., 1999) and GRANAT (Debrunner et al., 1992; 1993; 1997). Pion decay radiation together with observations of neutrons provide information on the highest ion energies produced during flares. Charged pions decay to yield electrons and positrons, which in turn produce gamma-rays by bremsstrahlung. Positrons also contribute to the continuum by annihilating in flight. Neutral pion decay results in two photons, one of which being emitted at high energies. This results in a very flat, broad 'bump' feature which has a maximum at 67 MeV. Synchrotron losses of electrons and positrons may be important and shorten the lifetime of electrons and positrons, therefore reducing their contribution with respect to the radiation from neutral pion decay (Murphy et al., 1987). Energetic electrons above 10 MeV are also produced in solar flares and produce bremsstrahlung continuum, potentially masking pion decay radiation.

Pion decay radiation was first observed with the SMM/GRS instrument for the flare of 3 June 1982 (Forrest et al., 1985).

TO BE COMPLETED

There are other subsections to be implemented

#### 0.5. PARTICLE POPULATIONS, ENERGETICS, AND RELATIONSHIP TO SEPs

TO BE IMPLEMENTED

#### 0.6. CHARACTERISTICS OF THE SOLAR ATMOSPHERE DURING FLARES FROM GAMMA-RAY LINE MEASUREMENTS

TO BE IMPLEMENTED